Eksergi
Chemical Engineering Journal
Vol 23, No. 1. 2026

ISSN: 1410-394X
e-ISSN: 2460-8203

Mechanistic Modeling of a Spiral-Wound Nanofiltration Module using DSPM-DE for High-Purity Salt Recovery from Desalination Brine

Mohamad Sugianto, Ali Altway, Susianto*

Department of Chemical Engineering, Faculty of Industrial Technology and Systems Engineering, Institut Teknologi Sepuluh Nopember, Surabaya, East Jawa, 60111, Indonesia

Artikel history:

Submitted 16 November 2025
Revision 25 November 2025
Accepted 6 December 2025
Online 13 December 2025

ABSTRACT: Rejected brine is a concentrated NaCl stream whose elevated Ca^{2+}, Mg^{2+}, and SO_4^{2-} depress the quality of industrial salt. We built a mechanistic model of a spiral-wound KeenSen NF1-4040F nanofiltration (NF) element using the Donnan–Steric Pore Model with Dielectric Exclusion coupled to the Extended Nernst–Planck equations. Radial transport is coupled to axial mass balances and solved at steady, isothermal conditions over $P_f = 2.5 - 12.5$ bar and $Q_{f,\mathrm{in}} = 1.08 - 3.60$ m^3 h^{-1}. Water flux J_w increases almost linearly with P_f; along the module $Q_f(z)$ falls and $Q_p(z)$ rises nearly linearly. Recovery increases with P_f but decreases with $Q_{f,\mathrm{in}}$. Flux decomposition shows cations are convention-dominated, whereas anions carry larger shares of diffusion and electromigration. Predicted end-of-module rejections are $SO_4^{2-}\approx$ 99.0-99.3%, $Mg^{2+}\approx$ 97.6-98.1%, $Ca^{2+}\approx$ 96.0-96.6%, $Cl^{-}\approx$ 88-89%, and $Na^{+}\approx$ 74-75%, confirming divalent $\gg$ monovalent selectivity. Linking to product quality, the simulated permeate at $P_f = 12.5$ bar and $Q_f = 2.34$ m^3 h^{-1} yields a conservative dry-salt purity of ~96.9 wt% NaCl when all non-halite salts co-precipitate. Under halite-first crystallization with a gypsum pre-step and bittern purge, only a minor fraction co-crystallizes, giving ≥98.5 wt% (≈99.5 wt% for a 20% co-crystallization assumption). Thus, operating at moderate-to-high P_f with moderate cross-flow not only maximizes recovery and divalent rejection but also supplies a permeate that can be crystallized to SNI-compliant high-purity salt.

Keywords: nanofiltration; rejected brine; DSPM-DE; divalent ions; high-purity salt

1. Introduction

Industrial salt is a key inorganic commodity used as a reactant, electrolyte, or processing aid in multiple sectors, including chlor-alkali production, food processing, textiles, leather, water treatment, and pharmaceuticals. In Indonesia, national demand for industrial-grade salt has been reported in the range of 3.8 - 4.0 million tonnes per year, while domestic production of high-purity salt remains structurally insufficient, so that a large share of demand is still met by imports. The chlor-alkali, glass, and related chemical industries account for the largest portion of this demand and require feed salt with high NaCl content and low levels of divalent cations such as Ca^{2+} and Mg^{2+} to avoid scaling, membrane fouling, and product quality problems (Hista Saputra et al., 2022). As a result, the development of alternative, higher-purity salt feedstocks is strategically important for reducing import dependence and improving the resilience of Indonesia's process industries.

One promising but underutilised source of concentrated brine is the reject stream from seawater desalination plants. Seawater desalination capacity has expanded rapidly worldwide, especially in arid and coastal regions, generating large volumes of high-salinity brine that are commonly discharged back to the marine environment. Global estimates suggest that desalination plants produce more than 140 million m³ of brine per day, often with salinity up to twice that of ambient seawater and containing process chemicals and trace metals (Jones et al., 2019; Omerspahic et al., 2022). If released without adequate management, this brine can increase salinity and temperature in the receiving waters, alter marine community structure, and degrade coastal ecosystems. At the same time, the high ionic strength and significant NaCl content of rejected brine make it an attractive candidate for valorisation pathways such as resource recovery and industrial salt production, in line with zero-liquid-discharge and circular-economy strategies (Omerspahic et al., 2022).

A key challenge in upgrading rejected brine to industrial-grade salt is the selective removal of divalent cations such as Ca^{2+} and Mg^{2+}, which promote hygroscopicity, caking, and scaling, and thus reduce the usability of the product in chlor-alkali and other sensitive processes. Membrane nanofiltration (NF) is particularly suited to this task because its separation characteristics lie between reverse osmosis (RO) and ultrafiltration (UF): NF

*Corresponding Author
Email address: susianto@its.ac.id

typically operates at lower transmembrane pressures than RO, offers higher water flux, and exhibits strong preferential rejection of multivalent ions over monovalent ones (EL Idrissi et al., 2024; Izadpanah & Javidnia, 2012). Recent studies on NF treatment of RO brine and diluted seawater have reported 79 - 89% removal of total dissolved solids (TDS) and 96 - 98% removal of total hardness, with especially high retention of Ca^{2+} and Mg^{2+}, demonstrating the technology's potential as a pre-treatment or stand-alone step for brine valorisation and scale control (Ali, 2021; Izadpanah & Javidnia, 2012). NF has also been applied to desalination brines specifically to recover water and reduce scaling precursors, often achieving high divalent-ion rejection at moderate operating pressures and recoveries (Avramidi et al., 2025).

To design NF systems that can reliably upgrade rejected brine into a suitable salt feedstock, it is not sufficient to rely solely on empirical performance curves; a mechanistic understanding of transport and exclusion phenomena in charged nanopores is required (Yudhi Pamungkas et al., 2025). Over the past two decades, the Donnan Steric Pore Model combined with Dielectric Exclusion (DSPM-DE) has emerged as a comprehensive framework for describing ion and water transport in NF membranes. The model solves the Extended Nernst-Planck (ENP) equations for each ionic species, accounting for diffusion, convection, and electromigration within the pores, while representing ion partitioning at the membrane interface through Donnan electrostatic exclusion, steric hindrance, and a dielectric exclusion term based on Born solvation energy differences between the pore and the bulk solution (Agboola et al., 2015; Roy et al., 2017; Saavedra et al., 2024a). Classical work by Bowen and co-workers established the DSPM-DE formulation and highlighted the importance of dielectric exclusion for multivalent ions, while more recent contributions have extended the model to examine temperature effects, membrane charge and pore size distributions, and the separate roles of Donnan versus dielectric exclusion in controlling selectivity (Agboola et al., 2015; Saavedra et al., 2024a).

Recent studies have used DSPM-DE to analyse increasingly complex NF systems, including multicomponent feeds and composition-tailored membranes. Cevallos-Cueva and co-author., (2025), for example, applied DSPM-DE to nitrate-selective NF membranes and showed that dielectric exclusion and diffusion jointly dominate sulfate rejection, leading to very high SO_4^{2-} retention (≈96 - 99%) while allowing partial passage of NO_3^-; negative apparent rejection of nitrate was observed under certain conditions due to coupled transport phenomena. In a follow-up study, the same group investigated Na^+ / Mg^{2+} selectivity in interfacially polymerised NF membranes and demonstrated how variations in piperazine and trimesoyl chloride concentrations modify membrane charge density, pore structure, and ultimately the Na^+ / Mg^{2+} separation factor, again using DSPM-DE as the modelling backbone. These works illustrate how mechanistic modelling can connect membrane formulation, operating conditions, and multicomponent ion transport in a physically interpretable way.

However, most DSPM-DE-based studies to date focus on idealised conditions such as synthetic salt solutions, potable-water treatment, or specific pollutant removal, and only a limited number address real rejected brine compositions that include Na^+, Cl^-, Ca^{2+}, Mg^{2+}, and SO_4^{2-} at high salinity levels representative of seawater desalination plants (Izadpanah & Javidnia, 2012; Omerspahic et al., 2022). Furthermore, relatively few works explicitly couple the radial (pore-scale) transport description of DSPM-DE with axial mass-balance equations along spiral-wound modules to explore process-scale performance metrics such as recovery, concentration profiles, and trade-offs between divalent-ion rejection and energy consumption. As a result, there is still a need for mechanistic models that can (i) capture the selective removal of Ca^{2+} and Mg^{2+} from realistic rejected brine streams, (ii) resolve the contributions of diffusion, convection, and electromigration to overall ion transport, and (iii) provide operating maps that are directly useful for designing NF-based routes to high-purity industrial salt.

Accordingly, this study develops a steady-state, isothermal DSPM-DE / ENP model for a commercial spiral-wound NF element (KeenSen NF1-4040F) treating a realistic five-ion, high-salinity rejected brine (Na^+, Cl^-, Ca^{2+}, Mg^{2+}, SO_4^{2-}). Unlike single-salt analyses, the formulation couples radial ENP transport inside charged nanopores with axial mass balances, enabling spatially resolved predictions of permeate-water flux and per-ion rejection along the module. The framework further quantifies, for each ion and position, the relative shares of convection, diffusion, and electromigration, thereby clarifying *why* divalent ions are preferentially excluded. To make the results directly usable, we construct an operator-oriented map of the P_f - Q_f space that links stage recovery to product quality and delineates practical windows for high-purity salt production. Model outputs are triangulated against NF90-type reference data to ensure semi-quantitative plausibility. We hypothesize that moderate-to-high feed pressure combined with moderate cross-flow maximizes divalent-ion rejection by strengthening dielectric exclusion while limiting concentration polarization, supporting the upgrading of rejected brine into a high-purity salt feedstock.

2. Materials and Methods

2.1 Modeled System and Operating Conditions

The nanofiltration (NF) module is represented as an equivalent flat "unwound" leaf of a spiral-wound KeenSen NF1-4040F element. Cross-flow occurs along the axial coordinate $z \in [0, L]$ in the feed channel, while solvent and ion transport through the active layer are resolved in the radial coordinate $x \in [0, \delta_x]$. The electrolyte contains five ionic species, Na^+, Cl^-, Ca^{2+}, Mg^{2+}, and SO_4^{2-}, which are assumed to satisfy local electroneutrality everywhere inside the pore solution. Steady-state, isothermal conditions ($T = 298.15$ K) are imposed, with the brine treated as an incompressible Newtonian fluid of constant bulk density and viscosity over the operating range, consistent with

ISSN: 1410-394X
e-ISSN: 2460-8203

mechanistic NF models for spiral-wound leaves in the literature (Bowen & Welfoot, 2002; Roy et al., 2015).

The feed composition is based on a representative rejected brine stream. On a molar concentration basis (mol·m^{-3}), the inlet feed contains Na^+ = 466.01, Cl^- = 681.04, Ca^{2+} = 7.78, Mg^{2+} = 38.99, and SO_4^{2-} = 31.80. The bulk solution density and viscosity are taken as $\rho = 1030.6$ kg·m^{-3} and $\mu = 1.96$ mPa·s, respectively, while the Stokes radii and bulk diffusivities for each ion follow low-pressure NF characterization work (Labban et al., 2017; Suhalim et al., 2022).

Operating conditions span a practical window for brine valorization. The feed pressure P_f is varied between 2.5, 5.0, 7.5, 10.0, and 12.5 bar (absolute), while the inlet feed flow rate $Q_{f,\text{in}}$ ranges from 1.08 to 3.60 m^3·h^{-1}. The permeate pressure P_p is maintained at 1.01325 bar. These conditions cover moderate-pressure NF typical of brine polishing and divalent–monovalent fractionation, comparable to recent RO-brine NF studies where divalent hardness and sulfate are selectively removed (Ali, 2021; Figueira et al., 2023a).

2.2 Physical Parameters and Osmotic Pressure

Membrane and module parameters are chosen to represent a commercial spiral-wound NF element in desalination pre-/post-treatment. The active layer is modeled as a charged, cylindrical-pore medium with effective pore radius $r_{\text{pore}} \approx 0.43$ nm and active-layer thickness $\delta_x = 1\,\mu$m, while the fixed volumetric charge density is set to $C_x \approx -45$mol·m^{-3}, typical for negatively charged thin-film composite NF membranes operating with multi-ionic brines (Cevallos-Cueva et al., 2024; Ma et al., 2014). The effective membrane area per element is $A_{\text{mem}} = 7.2$ m^2, the module length is $L = 1.016$ m, and the feed-channel hydraulic height is $d_h = 100\,\mu$m, which yields an equivalent channel cross-section $A_{\text{ch}} \approx A_{\text{mem}} L^{-1} = 7.09 \times 10^{-4}$ m^2.

Permeate-water flux J_w is computed from a Poiseuille-type relation for flow through the active layer,

$$J_w = K_{\text{perm}}\left[\left(P_f - P_p\right) - f\,\Delta\pi\right], \tag{1}$$

where the hydraulic permeability is

$$K_{\text{perm}} = \frac{r_{\text{pore}}^2}{8\mu\,\delta_x} \approx 1.18 \times 10^{-11}\ \text{m Pa}^{-1}\text{s}^{-1}, \tag{2}$$

and $f \in [0,1]$ is an effective osmotic factor used to interpolate between a purely hydraulic response ($f = 0$) and the full osmotic pressure difference $\Delta\pi$. Similar forms for J_w are standard in DSPM-DE-based NF models for charged membranes (Bowen & Welfoot, 2002; Saavedra et al., 2024).

The osmotic pressure difference is evaluated from the wall concentrations on the feed and permeate sides obtained from the concentration-polarization (CP) model. For each side s (feed or permeate), the solution osmotic pressure is approximated using a van 't Hoff expression,

$$\pi_w^{(s)} = RT \sum_i \nu_i C_{i,w}^{(s)}, \tag{3}$$

and the driving osmotic difference is

$$\Delta\pi = \pi_w^{(\text{feed})} - \pi_w^{(\text{perm})}. \tag{4}$$

Here R is the universal gas constant, $T$is the absolute temperature, ν_i is the van 't Hoff factor for ion i, and $C_{i,w}^{(s)}$ is the wall concentration at side s. This formulation is widely used in mechanistic NF analyses of multi-ionic brines and SWRO retentates (Labban et al., 2017; Micari et al., 2020).

To address robustness in the absence of in-house characterization, we add an analytical sensitivity rationale. From (2), $K_{\text{perm}} \propto r_{\text{pore}}^2$, so a +10% change in r_{pore} implies ≈ +21% in K_{perm} (and hence a comparable first-order increase in J_w and stage recovery if all else is fixed). Steric partitioning for a solute of hydrated radius a_i scales as $\Phi_i \approx (1-\lambda_i)^2$with $\lambda_i = a_i/r_{\text{pore}}$; thus $r_{\text{pore}} \uparrow$ reduces steric exclusion and tends to lower %rejection, most noticeably for larger / multivalent ions (Bowen & Welfoot, 2002). Conversely, increasing $|\,C_x\,|$ strengthens Donnan exclusion, roughly via $K_i \sim \exp(-z_i F\psi_D/RT)$ with ψ_D increasing with $|\,C_x\,|$, so anion rejection (Cl^-, SO_4^{2-}) increases, while cation response reflects a balance of convection vs. electromigration (Cevallos-Cueva et al., 2025; Saavedra et al., 2024a). These analytical trends are consistent with published DSPM-DE sensitivities and with the semi-quantitative NF90 sanity-check, indicating that our main conclusions (high divalent rejection at moderate–high P_f with moderate cross-flow) are robust to ±10% uncertainty in $r_{\text{pore}}$and C_x.

2.3 Radial Transport Model (DSPM-DE + ENP)

Ion transport inside the charged pores is described by the Donnan Steric Pore Model with Dielectric Exclusion (DSPM-DE), written in the framework of the Extended Nernst-Planck (ENP) equation. The total molar flux of ion i, J_i, is the sum of convection, diffusion, and electromigration,

$$J_i = K_{ic}\,C_i\,J_w - D_i^e\,\frac{dC_i}{dx} - \frac{z_i F}{RT}\,D_i^e\,C_i\,\frac{d\psi}{dx}, \tag{5}$$

where K_{ic} is a convective hindrance factor, $D_i^e = K_{id} D_{i,\infty}$ is the effective diffusivity in the pore (with K_{id} a diffusive hindrance factor and $D_{i,\infty}$ the bulk diffusivity), z_i is ion valence, $F$is Faraday's constant, and $\psi(x)$ is the dimensionless electrostatic potential. This formulation follows earlier DSPM-DE developments for NF membranes treating multi-ion solutions (Bandini & Vezzani, 2003; Bowen & Welfoot, 2002; Szymczyk et al., 2009).

Concentration polarization at the feed-side wall is accounted for through a film model. For each ion, the wall concentration on the feed side is

$$C_{i,w} = C_{i,\text{bulk}} \exp\left(\frac{J_w}{k_m}\right), \tag{6}$$

where the mass-transfer coefficient $k_m$is obtained from a Sherwood correlation,

$$k_m = \frac{\text{Sh}\, D_{i,\infty}}{d_h}, \;\; \text{Sh} = 0.079\, \text{Re}^{0.8}\, \text{Sc}^{0.33}, \tag{7}$$

with Reynolds and Schmidt numbers defined in the usual way from local channel hydrodynamics. Such CP correlations are commonly used in NF modeling for desalination and brine management (Suhalim et al., 2022)
Ion partitioning at the membrane interfaces is described by Donnan equilibrium combined with steric and dielectric exclusion. On each side $s \in \{\text{feed}, \text{perm}\}$, the concentration at the membrane side of the interface is

$$C_{i,\text{mem}}^{(s)} = \Phi_i\, \Phi_{B,i}\, C_{i,w}^{(s)} \exp\left(-\frac{z_i F}{RT}\, \psi_D^{(s)}\right), \tag{8}$$

where $\Phi_i = (1 - \lambda_i)^2$ is the steric partition coefficient with $\lambda_i = r_i / r_{\text{pore}}$, $\Phi_{B,i}$ is a Born factor accounting for the dielectric contrast between bulk solution and pore fluid, and $\psi_D^{(s)}$ is the Donnan potential at side s. The Donnan potentials are obtained from electroneutrality at each membrane interface,

$$\sum_i z_i C_{i,\text{mem}}^{(s)} + C_x = 0. \tag{9}$$

Inclusion of $\Phi_{B,i}$ implements dielectric exclusion in the sense of DSPM-DE and has been shown to be essential to capture multivalent-ion rejection in NF and negative rejections in certain co-ion systems (Bandini & Vezzani, 2003; Cevallos-Cueva et al., 2024; Saavedra et al., 2024a).

Equations (5), together with electroneutrality in the pore and the expression for J_w, define a coupled system of ordinary differential equations (ODEs) for $\psi(x)$ and $C_i(x)$ across the active layer. Boundary conditions are set by the interface concentrations and Donnan potentials: $\psi(0) = \psi_D^{(\text{feed})}$, $C_i(0) = C_{i,\text{mem}}^{(\text{feed})}$, $\psi(\delta_x) = \psi_D^{(\text{perm})}$, and $C_i(\delta_x) = C_{i,\text{mem}}^{(\text{perm})}$. The Donnan potentials $\psi_D^{(s)}$ are obtained by solving Eq. (9) via root-finding at each interface. This approach follows recent mechanistic DSPM-DE analyses for nitrate-selective and brine-treatment NF membranes (Cevallos-Cueva et al., 2024; Ghorbani et al., 2021).

2.4 Axial Module Model and Performance Indicators

Figure 1 illustrates the equivalent "unwound" flat-sheet representation of the spiral-wound nanofiltration element used in this work. The membrane leaf has length $L$and width W, with a thin active layer of thickness Δx separating the feed channel (height h_f) from the permeate channel (height h_p). Feed solution enters at $z = 0$ with volumetric flow rate $Q_{f,\text{in}}$ and bulk concentrations $C_{i,\text{in}}$, while permeate is collected along the permeate channel and exits at $z = L$ with flow rate $Q_p(L)$. The schematic also highlights the local solvent flux $J_w(z)$ and solute fluxes $J_i(z)$ across the membrane, which couple the radial transport model to the axial mass balances. This geometric idealization follows the flat-sheet / spiral-wound formulation used in large-scale DSPM-DE simulations of seawater nanofiltration (Roy et al., 2015).

For numerical solution, the module is discretized into Naxial control volumes of equal length $\Delta z = L/N$. Each segment k(with axial coordinate z_k) is associated with a membrane area

$$A_{\text{seg}} = \frac{A_{\text{mem}}}{L}\, \Delta z \tag{10}$$

where A_{mem} is the total active membrane area of the element. Within each segment, the radial DSPM-DE model provides the local solvent flux $J_w(k)$ and ion fluxes $J_i(k)$, which are assumed uniform over A_{seg} for that segment. This finite-volume coupling between local pore transport and axial bulk flow is standard in mechanistic NF simulations and has been successfully applied to multi-ionic feeds such as seawater and ion-exchange regenerant solutions (Micari et al., 2020; Roy et al., 2015).

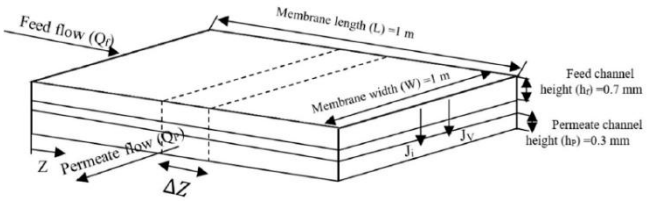

Figure 1. Schematic of the equivalent flat-sheet representation of the spiral-wound NF leaf, showing membrane length L, width W, active-layer thickness Δx, feed and permeate channel heights (h_f and h_p), and the axial variation of feed and permeate flow rates $Q_f(z)$ and $Q_p(z)$. Adapted from Roy et al. (2015)

The axial water-flow balances for feed and permeate streams across segment $k \to k + 1$are written as

$$Q_f^{(k+1)} = Q_f^{(k)} - J_w^{(k)} A_{\text{seg}} \tag{11a}$$

$$Q_p^{(k+1)} = Q_p^{(k)} + J_w^{(k)} A_{\text{seg}} \tag{11b}$$

where $Q_f^{(k)}$ and $Q_p^{(k)}$ are the segment-inlet flow rates of the feed and permeate, respectively. These relations enforce conservation of water: the volume that permeates through the membrane in each segment is subtracted from the feed channel and added to the permeate channel. Similar axial balance formulations are widely used in spiral-wound NF and RO modeling to capture the gradual increase of recovery and concentration along the feed path.

For each ionic species i, the discrete component mass balances in the retentate and permeate channels over segment k are formulated to match the thesis model exactly. The retentate balance is

$$C_{i,R}^{(k+1)} = C_{i,R}^{(k)} + \frac{-J_i^{(k)} A_{\text{seg}} - C_{i,R}^{(k)} (Q_f^{(k+1)} - Q_f^{(k)})}{\max\left(10^{-30}, Q_f^{(k)}\right)}, \tag{12}$$

ISSN: 1410-394X
e-ISSN: 2460-8203

and the permeate balance is

$$C_{i,P}^{(k+1)} = C_{i,P}^{(k)} + \frac{J_i^{(k)} A_{\text{seg}} - C_{i,P}^{(k)} (Q_p^{(k+1)} - Q_p^{(k)})}{\max(10^{-30}, Q_p^{(k)})}, \quad (13)$$

Here $C_{i,R}^{(k)}$ and $C_{i,P}^{(k)}$ are the bulk concentrations of species $i$in the retentate and permeate channels at the inlet of segment k, and the small denominator cut-off avoids numerical division by zero at the module inlet. The first term in each numerator accounts for the net radial flux $J_i^{(k)} A_{\text{seg}}$, while the second term represents dilution or concentration effects caused by the axial change in volumetric flow. This discrete formulation is equivalent to integrating the differential component balances along $z$under the assumptions of plug flow and negligible axial dispersion, which are typical for cross-flow nanofiltration modules (Bowen & Welfoot, 2002).

At the module outlet $z = L$, two key performance indicators are evaluated. The stage recovery is defined as

$$\text{Rec} = \frac{Q_p(L)}{Q_{f,\text{in}}} \quad (14)$$

which measures the fraction of the incoming feed converted to permeate. The overall rejection of ion $i$is calculated from the ratio of outlet molar flow rates in the permeate and retentate streams,

$$\%R_i = 100\left[1 - \frac{\dot{n}_{i,P}(L)}{\dot{n}_{i,R}(L)}\right], \quad (15)$$

$$\dot{n}_{i,P}(L) = Q_p(L)\, C_{i,P}(L), \quad (16a)$$

$$\dot{n}_{i,R}(L) = Q_f(L)\, C_{i,R}(L). \quad (16b)$$

These definitions are consistent with common practice in NF modeling and experimental characterization, facilitating comparison with literature data on multi-ionic separations and on the performance of commercial nanofiltration membranes (Ghorbani et al., 2021; Micari et al., 2020).

2.5 Numerical Solution Strategy and Model Verification

The DSPM-DE + ENP system in the radial coordinate is solved using MATLAB's explicit ODE45 solver, an adaptive Runge-Kutta (4, 5) method, with relative and absolute tolerances set to $10^{-7}$and 10^{-9}, respectively. For each axial segment, the CP correlation is evaluated from the local cross-flow conditions, the Donnan potentials at both interfaces are obtained from Eq. (9) via a scalar root-finding routine, and the resulting initial conditions are used to integrate the ODE system for $\psi(x)$ and $C_i(x)$ across the active layer. The resulting $J_w^{(k)}$ and $J_i^{(k)}$are then passed to the axial marching scheme (Eqs. (11) - (13)) to advance from segment $k$to $k+1$ until $z = L$. This iterative CP-Donnan-ODE coupling per segment is consistent with recent DSPM-DE implementations for spiral-wound NF modules (Ghorbani et al., 2021; Roy et al., 2015).

At the module inlet, initial conditions are set to $Q_f(0) = Q_{f,\text{in}}$, $Q_p(0) = 0$, $C_{i,R}(0) = C_{i,\text{feed}}$, and $C_{i,P}(0) = 0$. In selected scenarios, an effective osmotic factor f is calibrated by bisection within a bounded interval $[0, f_{\max}]$ to match a target overall recovery (e.g., 15%) with a tolerance of 5×10^{-4}. For pure hydraulic tests, $f$is set to zero in Eq. (1) to highlight the linear response of J_w to P_f. Similar strategies have been used to tune effective osmotic contributions in NF simulations of brine-valorization trains (Labban et al., 2017; Roy et al., 2015).

Internal verification includes (i) approximately linear J_w - P_f behavior in the purely hydraulic limit, (ii) overall mass balance closure with total mass-flow discrepancies well below 0.1%, (iii) absence of negative values for concentrations or flow rates, and (iv) physically consistent axial trends (monotonic decrease of $Q_f(z)$, increase of $Q_p(z)$, and progressive concentration of $C_{i,R}(z)$). External validation is performed by comparing predicted recoveries and ion rejections against data and trends from NF studies on RO brines and multi-ionic feeds of comparable salinity and composition (Ali, 2021; Cevallos-Cueva et al., 2024; Ghorbani et al., 2021; Micari et al., 2020).

3. Results & Discussion

3.1 Hydrodynamic Behaviour: Water-Flux Response to Feed Pressure and Module Mass Balance

We first verify that the simulated hydraulics of the KeenSen NF1-4040F element behave in a physically consistent way. Figure 2 shows the permeate-water flux J_w as a function of feed pressure P_f in the range 2.5 - 12.5 bar for a representative inlet flow rate.

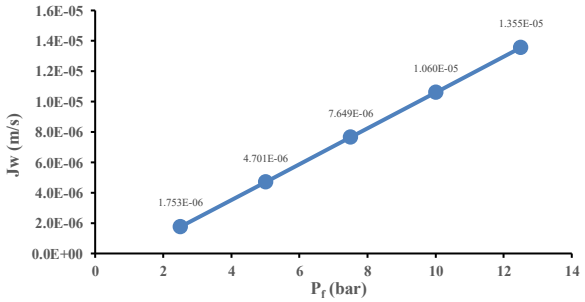

Figure 2. Solvent flux J_w (m/s) against P_f (bar) in hydraulic test.

The model predicts an almost linear increase of J_w with P_f, which reflects a nearly constant hydraulic permeability L_p and limited membrane compaction within this pressure window. This behaviour is in line with experimental nanofiltration studies, where pure-water flux is typically proportional to the effective transmembrane pressure until either compaction or strong concentration-polarization effects appear (Shahgodari et al., 2023).

Beyond the local flux–pressure relation, it is important to check whether the axial variation of the bulk flow rates remains consistent with overall mass conservation. Figure 3 illustrates the axial profiles of the retentate flow rate $Q_f(z)$ and permeate flow rate $Q_p(z)$ along the dimensionless module length z/L for selected combinations of P_f and inlet flow rate $Q_{f,\mathrm{in}}$. As water permeates through the membrane, $Q_f(z)$ decreases monotonically while $Q_p(z)$ increases, and both trends are close to linear under conditions where J_w is nearly uniform. This pattern confirms that the discretised model correctly couples the radial transport across the membrane with the longitudinal mass balance, similar to other axial-discretisation approaches for nanofiltration modules used in process design and optimisation (Hubach et al., 2023).

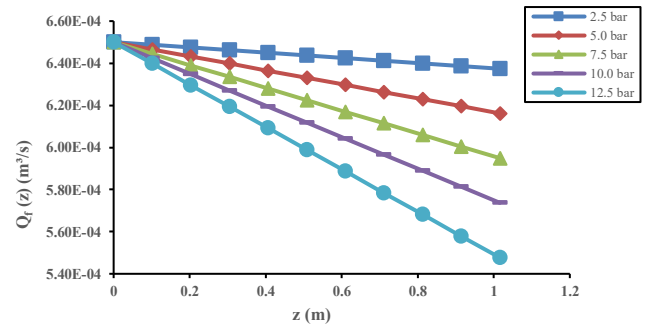

(a)

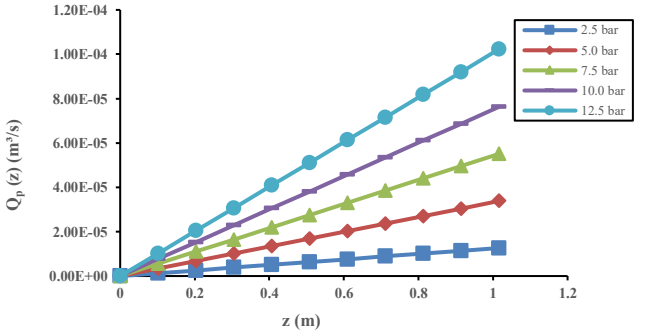

(b)

Figure 3. Axial hydrodynamic behaviour of the NF module at $Q_{f,\mathrm{in}} = 2.34\ \mathrm{m^3h^{-1}}$ for different feed pressures P_f: (a) retentate flow rate $Q_f(z)$; (b) permeate flow rate $Q_p(z)$

Taken together, Figures 2, 3(a), and 3(b) provide a hydrodynamic "sanity check" for the model: the element behaves as expected for a spiral-wound NF module operated in cross-flow, with a nearly linear J_w - P_f relationship and smooth, monotonic evolution of Q_f and Q_p along the module, before moving on to more detailed analyses of recovery and ion-transport mechanisms in the following subsections.

3.2 Stage Recovery and Operating Window

Stage recovery is defined as the ratio between the permeate flow rate at the module outlet and the inlet feed flow rate, $\mathrm{Rec} = Q_p(L)/Q_{f,\mathrm{in}}$ (see Section 2.4). For a single-pass nanofiltration module operated at fixed hydraulic conditions, increasing the feed pressure P_f generally raises the solvent flux J_w, enlarges $Q_p(L)$, and therefore increases recovery. In contrast, increasing the inlet flow rate $Q_{f,\mathrm{in}}$ mainly affects the denominator in the recovery expression, so that higher cross-flow tends to lower the stage recovery at constant pressure. This qualitative behaviour is consistent with recent DSPM-DE based simulations and experiments on multi-ionic feeds, which report higher recoveries at larger transmembrane pressure but a systematic decrease in recovery as the feed flow or cross-flow velocity is increased (Ghorbani et al., 2021).

Figure 4 summarises the simulated end-of-module recovery as a function of $Q_{f,\mathrm{in}}$ for five feed-pressure levels (P_f = 2.5 - 12.5 bar). A horizontal dashed line marks the design target of 15% recovery. At fixed pressure, the recovery curves decrease non-linearly as $Q_{f,\mathrm{in}}$ is raised. The concave-down shape reflects the fact that, under the hydraulic scenario considered here, $Q_p(L)$ is controlled primarily by J_w and the available membrane area and is therefore only weakly dependent on $Q_{f,\mathrm{in}}$, whereas the denominator in $\mathrm{Rec} = Q_p(L)/Q_{f,\mathrm{in}}$ increases linearly with the feed flow. As a result, recovery approximately scales with $1/Q_{f,\mathrm{in}}$ at constant P_f, reproducing the "recovery decreases with increasing feed flow" trend reported for NF treatment of multi-ionic solutions operated at different cross-flow velocities (Ghorbani et al., 2021).

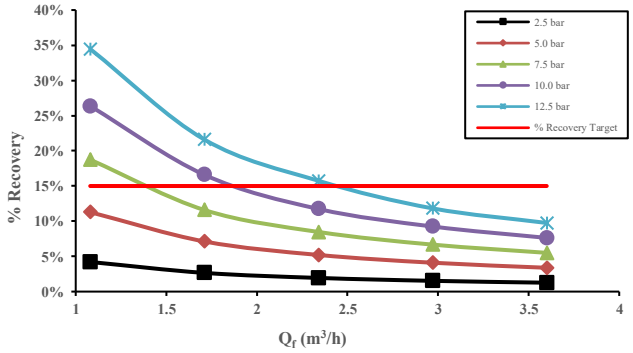

Figure 4. Simulated end-of-module recovery as a function of feed flow rate $Q_{f,\mathrm{in}}$ for different feed pressures P_f; the dashed line indicates the design target of 15% recovery

The second clear feature in Figure 4 is the upward shift of the entire recovery curve when P_f is increased. At the lowest feed flow ($Q_{f,\mathrm{in}} = 1.08\ \mathrm{m^3.h^{-1}}$), the model predicts final recoveries of approximately 4, 11, 19, 26, and 34% for P_f = 2.5, 5.0, 7.5, 10.0, and 12.5 bar, respectively. This monotonic increase is expected because higher pressure directly raises the driving force for solvent transport and thus the permeate production at fixed membrane area. Similar positive correlations between recovery and transmembrane pressure have been observed in long-term NF operation with ceramic and polymeric membranes, where recovery set-points between 40 - 80% are achieved by tuning the pressure

ISSN: 1410-394X
e-ISSN: 2460-8203

window while monitoring fouling and salt rejection (Cabrera et al., 2022).

The 15% target line in Figure 4 provides a practical operating map for the KeenSen NF1-4040F element treating rejected brine. According to the simulations, $P_f = 12.5$bar meets or exceeds the 15% recovery target up to approximately $Q_{f,\text{in}} \approx 2.4\ \text{m}^3.\text{h}^{-1}$, whereas $P_f = 10.0$bar satisfies the target up to $Q_{f,\text{in}} \approx 2.0\ \text{m}^3.\text{h}^{-1}$. At $P_f = 7.5$ bar, the target is only reached for relatively low feed flow rates ($Q_{f,\text{in}} \lesssim 1.5\ \text{m}^3.\text{h}^{-1}$), while 5.0 and 2.5 bar do not achieve 15% recovery within the investigated flow range. These trends align with NF design studies showing that higher pressure increases recovery but also strengthens concentration polarisation and the risk of scaling, whereas higher cross-flow mitigates polarisation at the cost of reduced single-pass recovery (Giacobbo et al., 2018).

Overall, the simulated recovery map indicates that the design target of 15% can be attained by combining moderately high feed pressures with moderate feed flow rates, while lower-pressure operation would require either longer modules or multi-stage configurations to reach similar overall recovery. This compact representation of the operating window serves as a convenient first-screening tool before moving to more detailed analyses of ion transport, concentration profiles, and rejection performance in the following subsections (Ghorbani et al., 2021; Giacobbo et al., 2018).

3.3 Ion Rejection Performance: Divalent vs. Monovalent

Ion rejection is used as a compact metric for how effectively the nanofiltration membrane retains each species relative to its passage into the permeate stream. In this work, end-of-module rejection for ion *i* is defined on a molar-flow basis at the outlet segment, which is equivalent to the more common concentration–based form $100\ (1 - C_{i,P}/C_{i,F})$when the bulk volumetric flow is nearly constant. This definition is consistent with recent NF studies that treat rejection as a module-scale performance indicator directly linked to the mass balance of each ionic species (Thabo et al., 2021). Over the investigated operating window, the simulated end-of-module rejections fall into a clear hierarchy, with divalent ions strongly favoured over monovalent ions (Table 1).

The ordering $SO_4^{2-} > Mg^{2+} \gtrsim Ca^{2+} \gg Cl^- > Na^+$ reflects the combined action of steric hindrance, Donnan exclusion and dielectric exclusion in the DSPM-DE framework. Divalent ions experience a stronger electrostatic and dielectric penalty when entering the narrow pores, while monovalent ions are less strongly repelled and therefore display lower rejections.

This divalent ≫ monovalent pattern, together with improved rejection at higher cross-flow velocities, is consistent with recent ENP-based modelling and experimental work on charged NF membranes, which show that charge selectivity and dielectric exclusion dominate the separation of multi-ionic brines in the typical NF pore-size range (Lu et al., 2022; Popova et al., 2023; Saavedra et al., 2024a).

Table 1. Simulated end-of-module rejection ranges for each ion (baseline operating window)

Ion	Charge	%Rejection
Na^+	+1	74 – 75 %
Cl^-	-1	88 – 89 %
Ca^{2+}	+2	96.0 – 96.6 %
Mg^{2+}	+2	97.6 – 98.1 %
SO_4^{2-}	-2	99.0 – 99.3 %

For the monovalent cations and anions, Na^+ and Cl^-, the model predicts moderate rejections of ≈74 - 75% and ≈88 - 89%, respectively. Na^+ is the least rejected ion because it experiences the weakest combination of steric and electrostatic exclusion; its small hydrated radius and single positive charge make convective transport with the solvent flux the dominant mechanism, so that increases in transmembrane pressure tend to enhance Na^+ advection more than they enhance its electrostatic repulsion. Consequently, at fixed feed flow rate, raising feed pressure can slightly decrease the apparent Na^+ rejection in the low-to-moderate pressure region, a behaviour also reported in NF studies of saline and surface waters when concentration-polarisation is not fully controlled (Tonova et al., 2020). In contrast, increasing the cross-flow rate $Q_{f,in}$ systematically improves Na^+ and Cl^- rejection by thinning the concentration-polarisation layer, lowering wall concentrations and moving the system closer to the intrinsic selectivity of the membrane; this trend aligns with hydrodynamic analyses that link higher cross-flow velocities to reduced CP and improved salt rejection (Lai et al., 2021; Tonova et al., 2020).

The divalent cations Ca^{2+} and Mg^{2+} exhibit significantly higher rejections, in the ranges 96.0 - 96.6% and 97.6 - 98.1%, respectively. Their larger hydrated radii increase steric hindrance, while the double positive charge leads to stronger Donnan exclusion at the negatively charged membrane surface, so that only a small fraction of the incoming flux is transmitted to the permeate. As cross-flow increases, the benefit of reduced concentration-polarisation is more modest than for monovalent ions because Ca^{2+} and Mg^{2+} are already strongly excluded by charge and dielectric effects; nevertheless, the simulations indicate a slight upward shift of rejection with $Q_{f,in}$, in line with experimental reports for brackish-water NF where divalent hardness ions remain > 95% rejected across a wide hydrodynamic window (Saavedra et al., 2024a). These results confirm that, within the investigated conditions, nanofiltration can consistently suppress Ca^{2+} and Mg^{2+} to levels suitable for high-purity salt production.

Sulfate (SO_4^{2-}) is the most strongly rejected species, with predicted rejections of 99.0 - 99.3% across the baseline operating window. This behaviour is characteristic of multivalent anions in charged NF membranes, for which dielectric exclusion and Donnan partitioning act

synergistically: the high valence and relatively large hydrated size of SO_4^{2-} create a substantial Born-energy penalty when moving from the high-dielectric bulk solution into the lower-dielectric pore environment, in addition to electrostatic repulsion by the negatively charged membrane matrix. Modern DSPM-DE studies emphasise that, for such anions, adjusting membrane charge density and pore dielectric constant is more effective for improving separation than simply increasing operating pressure, especially at intermediate–high salinity where Donnan exclusion alone is insufficient (Bargeman et al., 2023; Lu et al., 2022).

The very high SO_4^{2-} rejection predicted here is therefore consistent with the mechanistic understanding of NF and supports the feasibility of using the modelled module to strongly suppress sulfate impurities in rejected-brine feeds.

Overall, the rejection results summarised in Table 3 confirm that the KeenSen NF1-4040F module, operated within the investigated pressure and cross-flow window, behaves as a "hardness- and sulfate-selective" NF unit: divalent ions are almost completely retained, while monovalent ions are only partially rejected. This selectivity pattern matches the design objectives of producing higher-purity salt from rejected brine, where Ca^{2+}, Mg^{2+} and SO_4^{2-} are the primary impurities that must be minimised to avoid hygroscopicity and scaling issues in downstream industrial applications (Popova et al., 2023; Saavedra et al., 2024a).

3.4 Projected Product Purity from Permeate Composition (Linking to Industrial-Salt Specifications)

To connect the mechanistic NF results with practical salt quality, the simulated permeate composition at a representative operating point (here $P_f = 12.5$ bar, $Q_f = 2.34\ \mathrm{m^3\ h^{-1}}$) was translated into a projected "dry-salt" composition after complete water removal. Table 2 summarizes the simulated ion concentrations ($\mathrm{mol.m^{-3}}$) in the retentate and permeate that are used in this calculation.

Table 2. Simulated ion concentrations ($\mathrm{mol.m^{-3}}$) at $P_f = 12.5$ bar, $Q_f = 2.34\ \mathrm{m^3\ h^{-1}}$.

Stream	Na^+	Cl^-	Ca^{2+}	Mg^{2+}	SO_4^{2-}
Retentate	466.007	681.044	7.784	38.996	31.803
Permeate	125.291	82.021	0.288	0.823	0.247

Starting from this permeate, a conservative stoichiometric mapping was applied that forces all available counter-ions to precipitate as neutral salts in the following order (1) Chloride pairs first with Ca^{2+} and Mg^{2+} to form $CaCl_2$ and $MgCl_2$, (2) Any remaining Cl^- then pairs with Na^+ to form NaCl (3) Sulfate pairs with Na^+ to form Na_2SO_4.

This mapping deliberately maximizes the precipitation of non-halite salts ($CaCl_2$, $MgCl_2$, Na_2SO_4), thereby giving a lower-bound estimate of NaCl purity. Using the permeate-side moles and molar masses ($\mathrm{g\ mol^{-1}}$) of NaCl 58.44, $CaCl_2$ 110.98, $MgCl_2$ 95.21, and Na_2SO_4 142.04, the resulting dry-salt composition becomes:

- $CaCl_2$: limited by $Ca^{2+} \rightarrow 0.288$ mol $\rightarrow$ 32.1 g
- $MgCl_2$: limited by $Mg^{2+} \rightarrow 0.823$ mol $\rightarrow$ 78.4 g
- Remaining Cl^- goes to NaCl: $82.021 - 2 \times 0.288 - 2 \times 0.823 = 79.812$ mol $\rightarrow$ 4666 g
- SO_4^{2-} pairs with $Na^+ \rightarrow 0.247$ mol $\rightarrow$ 35.1 g

The corresponding mass fractions are listed in Table 3.

Table 3. Projected "dry-salt" composition from permeate (conservative stoichiometry).

Component	Mass (g)	Mass Fraction (wt%)
NaCl	4666	96.95
$CaCl_2$	32.1	0.67
$MgCl_2$	78.4	1.63
Na_2SO_4	35.1	0.73
Total	4812	100.00

Under this deliberately conservative assumption, the projected halite purity is ~ 96.9 wt% NaCl. This already lies within or just below the NaCl ranges specified for industrial salt in Indonesian and international standards (typically ≥ 96 - 98.5 wt% depending on grade and application). Indonesian SNI standards for industrial salt (SNI 8207:2016; SNI 0303 series) commonly cite minimum NaCl contents in the 96 - 98.5% range for high-grade industrial and food-industry salts (Astuti et al., 2021; Banerjee et al., 2025). Field and laboratory studies on Indonesian salt production likewise use 98.5% NaCl as a benchmark for industrial-grade quality (Ojo & Oludolapo, 2025; Ridha et al., 2016).

However, this 96.9% value should be interpreted as a lower bound for two reasons. First, in practical solar-salt and evaporative crystallizer operations, halite (NaCl) tends to crystallize first, while the more soluble Mg^{2+}, SO_4^{2-}, and part of the Cl^- remain in the mother liquor (bittern). Subsequent stages or separate ponds then precipitate Mg- and sulfate-rich phases (e.g. $MgSO_4 \cdot xH_2O$, kainite, carnallite, gypsum) from this bittern stream (Astuti et al., 2021; Sri et al., 2023). Recent brine-valorization and salt-recovery studies explicitly note that NaCl crystallization produces a halite-rich solid product, while divalent ions are concentrated in the bittern, where they are better recovered as secondary products (Morgante et al., 2022). Second, nanofiltration pretreatment is now widely proposed as a divalent-ion barrier in RO and brine-mining schemes, exploiting the typical NF selectivity of "high Ca^{2+}/Mg^{2+} rejection, moderate NaCl passage" to prevent scaling while preserving most monovalent salt (Bagastyo et al., 2021; Ojo & Oludolapo, 2025). Pilot-scale and full-scale studies show that NF can remove >90 - 98% of Ca^{2+} and Mg^{2+} at modest pressures, enabling downstream crystallizers to operate with brines already depleted in divalent hardness and enriched in NaCl (Ojo & Oludolapo, 2025). In parallel, industrial salt-purification work using $NaOH/Na_2CO_3$ precipitation or multi-step recrystallization consistently reports that Ca and

ISSN: 1410-394X
e-ISSN: 2460-8203

Mg are preferentially removed as hydroxide, carbonate, or gypsum solids in upstream steps, with final NaCl purities ≥97 - 99% relative to SNI 8207 targets (Astuti et al., 2021; Ojo & Oludolapo, 2025; Rismana et al., 2024; Sri et al., 2023).

Interpreting our simulation in light of this process-realistic crystallization sequence leads to a more appropriate purity estimate. If the NF permeate is used as feed to a halite crystallizer that operates in "halite-first" mode (i.e. Mg^{2+}-rich bittern purge and gypsum control downstream), the crystal phase will be dominated by NaCl, while a significant fraction of $MgCl_2$ and Na_2SO_4 will remain in the mother liquor rather than co-crystallizing with halite. This behavior is consistent with reported observations for both seawater-derived saltworks and bittern-recovery schemes, where NaCl forms the primary crystalline product and Mg-/sulfate-rich phases are recovered as co-products from the bittern (Astuti et al., 2021; Bagastyo et al., 2021; Gilani et al., 2024).

To capture this effect in a simple way, a partition factor f can be introduced to represent the fraction of non-halite salts that incidentally co-crystallize with the NaCl product (with $1 - f$ remaining in the bittern). For example, if only $f = 0.20$ (20%) of $MgCl_2$ and Na_2SO_4 from Table 3 is assumed to enter the halite crystal phase, while 80% is rejected to the bittern, the projected crystal composition becomes:

- NaCl: still ≈ 4666 g
- Co-crystallized non-halite: $0.20 \times (78.4 + 35.1) \approx 22.7$ g

The corresponding NaCl mass fraction in the harvested salt is then:

$$w_{\mathrm{NaCl,crystal}} = \frac{4666}{4666 + 22.7} \approx 99.5\ \mathrm{wt\%},$$

which is well above the 98.5 wt% NaCl threshold typically cited for the highest industrial-salt grades in Indonesia (Astuti et al., 2021; Ojo & Oludolapo, 2025). Even for a more conservative case, where up to $f = 0.40$ of $MgCl_2$ and Na_2SO_4 were to co-crystallize with halite, the calculated NaCl purity would still exceed 98.5 wt%. Thus, once realistic halite-first crystallization and bittern management are accounted for, the NF permeate projected by our model is fully compatible with premium industrial-salt specifications.

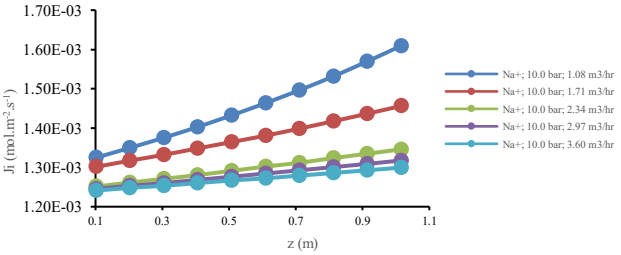

(a)

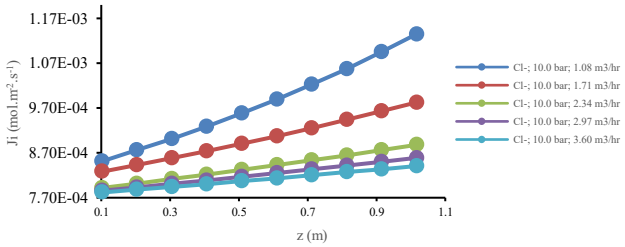

(b)

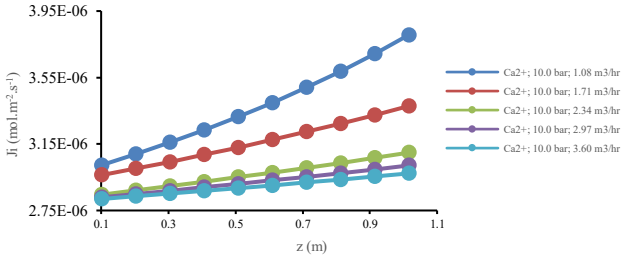

(c)

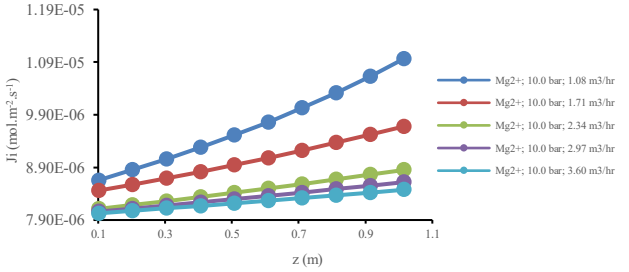

(d)

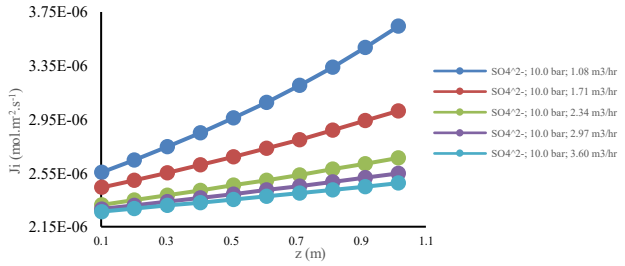

(e)

Figure 5. Simulated axial ionic flux profiles $J_i(z)$ at $P_f = 10.0$ bar for (a) Na^+, (b) Cl^-, (c) Ca^{2+}, (d) Mg^{2+}, and (e) SO_4^{2-} for different inlet feed flow rates $Q_{f,\mathrm{in}}$ (1.08–3.60 $m^3 \cdot h^{-1}$).

In short, the conservative stoichiometry in Table 3 demonstrates that the NF permeate is already suitable for producing at least ≈96 wt% NaCl upon simple evaporation, while a process-realistic crystallization interpretation, consistent with current brine-valorization and salt-purification practice, indicates that ≥98.5 wt% NaCl purity is achievable, thereby meeting and potentially exceeding SNI industrial-salt targets when standard crystallizer operation (gypsum control plus bittern purge) is applied downstream.

3.5 Axial Ion Fluxes and Concentration Profiles: Mechanistic Interpretation

To better understand the origin of the outlet rejection trends discussed in Section 3.3, this subsection examines the axial behaviour of ion fluxes and bulk concentrations along the NF module. Figure 5 shows the simulated axial profiles of the total ionic flux $J_i(z)$ for each species at a representative operating point (e.g. $P_f = 10$ bar and $Q_{f,\text{in}} = 2.34\ \text{m}^3.\text{h}^{-1}$). These fluxes are obtained from the Extended Nernst-Planck (ENP) equation with Donnan, steric, and dielectric exclusion (DSPM-DE), as outlined in Section 2. The ENP formulation decomposes J_i conceptually into convective, diffusive, and electromigrative contributions; in practice, the model results confirm that convection dominates the net transport of most cations, while diffusion and electromigration play more prominent roles for anions, in agreement with recent mechanistic NF studies (Cevallos-Cueva et al., 2024; Ghorbani et al., 2021).

As shown in Figure 5, all ions exhibit positive fluxes that increase monotonically with axial position. The profiles are almost linear over most of the module length, reflecting the combination of (i) a decreasing retentate flow rate $Q_f(z)$, which leads to progressive concentration build-up, and (ii) a nearly uniform permeate-water flux $J_w$under the hydraulic conditions considered here. Because the convective term in the pores is proportional to $J_w$and to the local wall concentration $C_{i,w}(z)$, the convective contribution grows as the solution becomes more concentrated towards the module outlet. Diffusion opposes this convective transport by driving ions from the concentrated retentate side towards the permeate, whereas the electromigrative term adjusts to preserve local electroneutrality. Similar axial trends in $J_i(z)$ have been reported in other DSPM-DE simulations for multicomponent feeds, confirming that the present framework captures the essential coupling between hydrodynamics, ion transport, and charge balance in spiral-wound NF elements (Ghorbani et al., 2021; Hubach et al., 2023).

The relative magnitude of J_i across species follows the selectivity hierarchy expected for a negatively charged polyamide NF membrane. Monovalent ions (Na^+, Cl^-) present the highest fluxes, with $J_{\text{Na}+}$ typically larger than J_{Cl^-} because Na^+ experiences weaker electrostatic exclusion and is strongly dragged by the permeate flow. In contrast, the fluxes of divalent ions (Ca^{2+}, Mg^{2+}, SO_4^{2-}) are substantially lower and increase more slowly with z. This is a direct consequence of stronger steric hindrance, Donnan exclusion, and dielectric exclusion for multivalent species, particularly SO_4^{2-}, which faces the largest Born-energy penalty when entering the lower-dielectric pore environment. These mechanistic features are consistent with reported pore-scale partition coefficients and mobilities from detailed DSPM-DE analyses of tight NF membranes (Cevallos-Cueva et al., 2024; Saavedra et al., 2024a).

Beyond the through-pore fluxes discussed above, the simulated axial bulk concentrations provide a complementary picture. Along the retentate channel, the model predicts that the retentate-side concentrations $C_{i,R}(z)$ of Na^+, Cl^-, Ca^{2+}, Mg^{2+}, and SO_4^{2-} increase monotonically with distance $z$as water is progressively removed, with steeper gradients at higher P_f and lower $Q_{f,\text{in}}$ where both recovery and concentration polarisation are stronger. In physical terms, the combined effect of solvent permeation and limited back-diffusion leads to enrichment of all ionic species near the module outlet. Permeate-side concentrations $C_{i,P}(z)$ remain much lower than $C_{i,R}(z)$ for the strongly rejected ions, SO_4^{2-} and Mg^{2+} stay at very low levels along the entire module, whereas Na^+ and Cl^- exhibit higher and more rapidly increasing $C_{i,P}(z)$. This behaviour is consistent with classical concentration-polarisation theory for NF/UF, which links retentate enrichment and mild flux decline to the build-up of solute in the boundary layer adjacent to the membrane surface (Giacobbo et al., 2018).

Taken together, the axial flux and concentration profiles predicted by the model provide a mechanistic explanation for the outlet rejection hierarchy summarised in Section 3.3. The strong build-up of $C_{\text{SO}_4^{2-},R}(z)$ and $C_{\text{Mg}^{2+},R}(z)$, combined with low permeate concentrations and relatively small fluxes for these ions, underpins the very high end-of-module rejections (≥97 - 99%) obtained for sulfate and magnesium. Conversely, the much larger convective fluxes and higher permeate concentrations of Na^+ and Cl^- naturally lead to lower overall rejections in the 70 - 90% range. Similar divalent ≫ monovalent selectivity and ion-specific axial trends have been reported in ENP/DSPM-DE studies of multi-ionic brines and seawater, reinforcing that the present modelling framework captures the relevant transport physics for nanofiltration of rejected brine in spiral-wound modules (Cevallos-Cueva et al., 2024; Ghorbani et al., 2021; Hubach et al., 2023).

3.6 Mechanistic Transport Decomposition and Model Validation

To better interpret the overall rejection behaviour, the total molar flux of each ionic species, J_i, was decomposed into the three contributions appearing in the Extended Nernst–Planck (ENP) equation, namely convection, diffusion, and electromigration. For a given operating condition, the local values of each mechanism were calculated across the membrane thickness and along the module length, then axially averaged to obtain representative percentages of $|J_{i,\text{conv}}|$, $|J_{i,\text{diff}}|$, and $|J_{i,\text{elec}}|$ relative to $|J_i|$. This approach follows earlier ENP / DSPM-DE studies that use flux decomposition to link ion-specific selectivity to hydrodynamics and electrostatic exclusion (Cevallos-Cueva et al., 2024; Ghorbani et al., 2021; Szymczyk et al., 2009).Table 4 summarises the axial-average contribution of each mechanism for Na^+, Cl^-, Ca^{2+}, Mg^{2+}, and SO_4^{2-} over the investigated pressure window $P_f = 2.5 - 12.5$ bar at $Q_{f,\text{in}} = 2.34\ \text{m}^3.\text{h}^{-1}$. For Na^+, convection clearly dominates the transport, contributing approximately 75 - 80 % of the total flux, while electromigration contributes about 17 - 22 % and diffusion less than about 4 % across the entire pressure range. Cl^- displays a more balanced behaviour, with convection contributing around 36 - 43 %, diffusion 34 - 37 %, and electromigration 23 - 28 %, reflecting its monovalent

ISSN: 1410-394X
e-ISSN: 2460-8203

charge and weaker Donnan exclusion compared to the divalent ions.

For Ca^{2+}, the convective contribution is also very strong (≈78 - 82 %), whereas diffusion and electromigration account for roughly 15 - 17 % and 4 - 5 %, respectively, consistent with strong electrostatic and dielectric exclusion that limit back-diffusion of this divalent cation. Mg^{2+} shows the highest sensitivity to pressure: convection decreases from about 84 % at 2.5 bar to ≈71 % at 12.5 bar, while diffusion increases from ~10 % to ≈28 - 29 %, and electromigration remains relatively small (≈1.4 - 1.7 %). Finally, SO_4^{2-} exhibits a more even split between convection and diffusion, with convective contributions decreasing from ~71 % to ~65 % and diffusion rising from ~23 - 24 % to ~26 - 27 % as pressure increases; electromigration for SO_4^{2-} lies in the range 6 - 8 %.

Table 4. Axial-average contribution of transport mechanisms to the total ionic flux for each species over $P_f = 2.5 - 12.5$ bar at $Q_{f,\text{in}} = 2.34\ \text{m}^3.\text{h}^{-1}$(percent ranges)

Ion	$J_{i,conv}$ (%)	$J_{i,diff}$ (%)	$J_{i,elec}$ (%)
Na^+	75 - 80	0 - 4	17 - 22
Cl^-	36 - 43	34 - 37	23 - 28
Ca^{2+}	78 - 82	15 - 17	4 - 5
Mg^{2+}	71 - 84	10 - 29	1 - 2
SO_4^{2-}	65 - 71	23 - 27	6 - 8

The patterns in Table 4 provide a mechanistic interpretation of the rejection hierarchy discussed in Sections 3.3 and 3.5. For Na^+ and Ca^{2+}, the flux is primarily convective, with only modest diffusive counter-flux; these ions are carried forward with the permeating water, leading to comparatively lower rejections for Na^+ and intermediate rejections for Ca^{2+}. In contrast, SO_4^{2-} and Mg^{2+} experience strong Donnan and dielectric exclusion, which suppresses convective transport and enhances diffusive back-transport, thereby supporting very high overall rejections despite significant enrichment in the retentate. The nearly balanced contributions of convection, diffusion, and electromigration for Cl^- are consistent with its role as the main counter-ion that maintains electroneutrality within the pores, a behaviour also reported in other multi-ionic DSPM-DE analyses of brines and seawater. From a modelling standpoint, this mechanistic decomposition is in good agreement with previous ENP / DSPM-DE applications, where convection typically dominates cation fluxes while anions, especially multivalent ones, show a larger share of diffusion and electromigration due to stronger electrostatic exclusion and the requirement of local electroneutrality (Ghorbani et al., 2021; Giacobbo et al., 2018; Szymczyk et al., 2009).

Model validation was carried out at two levels. First, internal numerical checks were performed to ensure the consistency of the coupled radial-axial solution: for all simulated conditions, global mass balances for water and each ionic species closed within tight numerical tolerances, and electroneutrality was satisfied in both retentate and permeate streams. The nearly linear relation between solvent flux $\boldsymbol{J_w}$ and transmembrane pressure in the hydraulic test (Section 3.1) further indicates that the hydraulic permeability and osmotic-pressure corrections are correctly implemented. Second, predictions were confronted with independent experimental data for nanofiltration of brines and multi-ionic electrolyte solutions using commercial polyamide tight-NF membranes.

In particular, the simulated trends, high rejection of divalent ions and lower rejection of monovalent ions, agree with reports for NF90 and similar membranes treating seawater / SWRO brines (Figueira et al., 2023b; Giacobbo et al., 2018; Saavedra et al., 2024). Beyond trend matching, we also anchored the model to a standard benchmark: the FilmTec NF90 datasheet reports stabilized $MgSO_4$ rejection ≥ 97% at 25 °C, 2,000 ppm $MgSO_4$, 70 psi (~4.8 bar) and ~15% recovery. At $P_f \approx 5$ bar with the inlet flow adjusted to achieve Rec ≈15%, our simulation gives $R_{Mg^{2+}}$= 97.8% and $R_{SO_4^{2-}}$= 99.1%, i.e., within 0 - 2 pp of the benchmark, while predicted NaCl rejections (R_{NA^+} ~ 74–75%, R_{Cl}~ 88–89%) remain consistent with the expected divalent ≫ monovalent selectivity under multi-ionic, higher-salinity feeds. Taken together, the mechanistic flux decomposition, internal numerical consistency, and point-wise agreement with NF90-type data indicate that the present DSPM-DE model provides a physically sound and semi-quantitatively reliable description of ion transport in the KeenSen NF1-4040F element treating rejected brine. Limitation: no new experiments were performed on the specific KeenSen module; full quantitative calibration (e.g., direct measurement of r_{pore}, C_x, and single-salt trials) is left for future work ((Figueira et al., 2023; FilmTecTM Membranes FilmTecTM NF270 Nanofiltration Elements for Commercial Systems, 2021; Giacobbo et al., 2018; Saavedra et al., 2024).

4. Conclusions

This study developed and applied a coupled DSPM-DE/Extended Nernst–Planck model for a spiral-wound KeenSen NF1-4040F element treating multi-ionic rejected brine, with the aim of predicting water flux, recovery, and ion-specific rejection as a function of feed pressure and inlet flow rate. The hydraulic verification showed a nearly linear J_w - P_f relationship and consistent axial mass balances, confirming that the implemented permeability and pressure–drop relations are physically sound. The recovery maps revealed that a target single-pass recovery of around 15% can be achieved by combining moderate-to-high feed pressures with intermediate feed flow rates, while the axial profiles of concentrations and ionic fluxes clarified how retentate enrichment and through-pore transport evolve along the module. Mechanistic flux decomposition demonstrated that cation transport, especially Na^+ and Ca^{2+}, is strongly convection-dominated, whereas diffusion and electromigration contribute a larger fraction to anion transport, particularly for SO_4^{2-} and, to a lesser extent, Cl^-. As a result, the model reproduces a clear divalent ≫

monovalent selectivity, with very high rejections for SO_4^{2-}, Mg^{2+}, and Ca^{2+} and lower, but still significant, rejections for Na^+ and Cl^-, providing a coherent process-scale explanation for the observed separation hierarchy.

From an application perspective, these results support the use of nanofiltration as a selective pre-purification step to upgrade rejected brine into a higher-purity feed for industrial salt production, by strongly suppressing hardness and sulfate while allowing part of the NaCl to pass. At the same time, the study highlights key modelling limitations, such as the simplified treatment of osmotic effects and concentration polarisation, the assumption of ideal solution properties, and the neglect of fouling and ageing, that point to natural extensions of this work. Future research should incorporate more detailed CP correlations and osmotic-pressure corrections, calibrate membrane parameters via dedicated experiments and inverse modelling, and couple the transport model with energy and cost analyses to optimise P_f - $Q_{f,\mathrm{in}}$ - recovery trade-offs. In the longer term, extending the framework to multi-stage or recycle configurations and embedding fouling/aging dynamics would further enhance its value as a design and optimisation tool for valorising rejected brine in industrial salt supply chains.

Importantly, by translating the simulated permeate at a representative operating point ($P_f = 12.5$ bar, $Q_f = 2.34\ \mathrm{m^3\ h^{-1}}$) into a projected dry-salt composition, the analysis shows a conservative NaCl purity of ~96.9 wt% when all non-halite salts ($CaCl_2$, $MgCl_2$, Na_2SO_4) are forced to co-precipitate. Interpreted under a process-realistic crystallization sequence, gypsum control followed by halite-first crystallization with bittern purge, only a small fraction of non-halite salts co-crystallizes with halite; with a representative partition factor $f \approx 0.2$, the harvested crystal is ~99.5 wt% NaCl, and even $f \leq 0.4$ still yields ≥98.5 wt%, consistent with premium SNI industrial-salt specifications. These results bridge the mechanistic NF predictions to downstream salt quality, indicating that moderate-to-high P_f with moderate cross-flow not only meets recovery and rejection targets but also supplies a permeate that can be crystallized to SNI-compliant high-purity salt using standard gypsum-pre-step and bittern-management practice.

From an energy perspective, the recommended operating point at $P_f = 12.5$ bar and a design single-pass recovery of $R \approx 0.15$ corresponds to a stage-level specific energy consumption of approximately 2.8 - 3.0 $\mathrm{kWh \cdot m^{-3}}$ permeate, assuming a typical pump efficiency of 75% and no energy-recovery devices. This value falls within the upper range of reported SECs for nanofiltration units treating brines (≈0.7 - 3 $\mathrm{kWh \cdot m^{-3}}$, depending on pressure and recovery) and is comparable to the energy demand of modern SWRO systems, while the NF module in our scheme only polishes the rejected-brine side stream; hence, the incremental energy penalty for upgrading brine into an industrial-salt feed is moderate and can be further reduced in future work by multi-stage configurations or energy-recovery integration.

Acknowledgements

The authors gratefully acknowledge the Department of Chemical Engineering, Institut Teknologi Sepuluh Nopember (ITS), for providing the computational facilities and academic environment that supported this work. The first author would like to thank Dr. Ir. Susianto, DEA and Prof. Dr. Ir. Ali Altway, M.Sc. for their continuous guidance, constructive discussions, and supervision during the development of the mathematical model and the preparation of this manuscript.
This research was carried out as part of the Master's thesis of the first author at ITS. The authors also appreciate the technical and administrative assistance provided by colleagues in the graduate programme and laboratory staff.

Statement

This manuscript was edited for language clarity using AI-assisted tools (ChatGPT) under the direct supervision of the authors. No part of the scientific analysis, data processing, modelling, or interpretation was generated by AI. All scientific content, results, and conclusions were fully produced and verified by the authors.

Credit Authorship Contribution Statement

Mohamad Sugianto: Conceptualization, Methodology, Software, Validation, Formal analysis, Investigation, Data curation, Visualization, Writing – original draft, Writing – review & editing.
Susianto: Conceptualization, Methodology, Supervision, Project administration, Writing – review & editing.
Ali Altway: Conceptualization, Methodology, Supervision, Project administration, Funding acquisition, Writing – review & editing.

Declaration of competing interests

The authors declare that they have no known competing financial interests or personal relationships that could have appeared to influence the work reported in this paper.

Data availability

The data supporting the findings of this study, including simulation scripts and numerical outputs, are available from the corresponding author upon reasonable request.

References

Agboola, O., Maree, J., Kolesnikov, A., Mbaya, R., & Sadiku, R. (2015). Theoretical performance of nanofiltration membranes for wastewater treatment. In *Environmental Chemistry Letters* (Vol. 13, Issue 1, pp. 37–47). *Springer Verlag*. https://doi.org/10.1007/s10311-014-0486-y

Ali, M. E. A. (2021). Nanofiltration process for enhanced treatment of RO brine discharge. *Membranes*, *11*(3), 1–6. https://doi.org/10.3390/membranes11030212

Astuti, D. H., Purba, T., Su'udi, N., Sani, & Nugraha, R. E. (2021). *The Role of Na_2CO_3 as Precipitating Agent in*

ISSN: 1410-394X
e-ISSN: 2460-8203

Salt Purification Process. https://doi.org/10.11594/nstp.2021.1405

Avramidi, M., Loizou, C., Kyriazi, M., Malamis, D., Kalli, K., Hadjicharalambous, A., & Kollia, C. (2025). Optimization of the quality of reclaimed water from urban wastewater treatment in arid region: A zero liquid discharge pilot study using membrane and thermal technologies. *Membranes*, *15*(7). https://doi.org/10.3390/membranes15070199

Bagastyo, A. Y., Sinatria, A. Z., Anggrainy, A. D., Affandi, K. A., Kartika, S. W. T., & Nurhayati, E. (2021). Resource recovery and utilization of bittern wastewater from salt production: a review of recovery technologies and their potential applications. In *Environmental Technology Reviews* (Vol. 10, Issue 1, pp. 294–321). *Taylor and Francis Ltd*. https://doi.org/10.1080/21622515.2021.1995786

Bandini, S., & Vezzani, D. (2003). Nanofiltration modeling: The role of dielectric exclusion in membrane characterization. *Chemical Engineering Science*, *58*(15), 3303–3326. https://doi.org/10.1016/S0009-2509(03)00212-4

Banerjee, P., Zaneldin, E. K., Al-Marzouqi, A. H., & Ahmed, W. K. (2025). A review of reject brine disposal, management, and construction Applications. In *Buildings* (Vol. 15, Issue 13). *Multidisciplinary Digital Publishing Institute* (MDPI). https://doi.org/10.3390/buildings15132317

Bargeman, G., Guerra Miguez, O., Westerink, J. B., & ten Kate, A. (2023). Chloride retention model for concentrated solutions containing sodium chloride and sodium sulfate based on thermodynamic considerations. *Desalination*, *555*. https://doi.org/10.1016/j.desal.2023.116562

Bowen, W. R., & Welfoot, J. S. (2002). Modelling The performance of membrane nanofiltration - critical assessment and model development. In *Chemical Engineering Science* (Vol. 57). www.elsevier.com/locate/ces

Cabrera, S. M., Winnubst, L., Richter, H., Voigt, I., McCutcheon, J., & Nijmeijer, A. (2022). Performance evaluation of an industrial ceramic nanofiltration unit for wastewater treatment in oil production. *Water Research*, *220*. https://doi.org/10.1016/j.watres.2022.118593

Cevallos-Cueva, N., Rahman, M. M., Hailu Kinfu, H., & Abetz, V. (2024). Mass transport mechanism of nitrate selective nanofiltration membranes on the basis of The Donnan Steric Pore Model with Dielectric Exclusion (DSPM-DE). *Chemical Engineering Journal*, *493*. https://doi.org/10.1016/j.cej.2024.152775

Cevallos-Cueva, N., Rahman, M. M., Kinfu, H. H., & Abetz, V. (2025). Mass transport mechanisms insights of selective sodium / magnesium separation through nanofiltration membranes. *Journal of Membrane Science*, *721*. https://doi.org/10.1016/j.memsci.2025.123808

EL Idrissi, Y., Benabbou, M., Rais, Z., & EL Haji, M. (2024). Brackish and seawater pretreatment processes: A systematic literature review. *Desalination and Water Treatment*, *318*. https://doi.org/10.1016/j.dwt.2024.100350

Figueira, M., Rodríguez-Jiménez, D., López, J., Reig, M., Luis Cortina, J., & Valderrama, C. (2023). Evaluation of the nanofiltration of brines from seawater desalination plants as pre-treatment in a multimineral brine extraction process. *Separation and Purification Technology*, *322*. https://doi.org/10.1016/j.seppur.2023.124232

FilmTec™ Membranes FilmTec™ NF270 Nanofiltration Elements for Commercial Systems. (2021). www.dupont.com/water/contact-us

Ghorbani, A., Bayati, B., Drioli, E., Macedonio, F., Kikhavani, T., & Frappa, M. (2021). Modeling of nanofiltration process using dspm-de model for purification of amine solution. *Membranes*, *11*(4). https://doi.org/10.3390/membranes11040230

Giacobbo, A., Bernardes, A. M., Rosa, M. J. F., & De Pinho, M. N. (2018). Concentration polarization in ultrafiltration/nanofiltration for the recovery of polyphenols from winery wastewaters. *Membranes*, *8*(3). https://doi.org/10.3390/membranes8030046

Gilani, I. E., Hosseini, H., Al-Ghouti, M. A., Saadaoui, I., & Sayadi, S. (2024). Microalgal-based desalination brine remediation: Achievements, challenges, and future research trends. In *Environmental Technology and Innovation* (Vol. 34). Elsevier B.V. https://doi.org/10.1016/j.eti.2024.103592

Hista Saputra, I., Mariyanti, T., & Athallah, M. R. (2022). Strategy for development of pharmaceutical salt business in improving The welfare of The salt farmers from islamic perspective. *ADI Journal on Recent Innovation (AJRI)*, *4*(1), 43–55. https://doi.org/10.34306/ajri.v4i1.750

Hubach, T., Schlüter, S., & Held, C. (2023). Model-based optimization of multi-stage nanofiltration using the solution-diffusion-electromigration Model. *Processes*, *11*(8). https://doi.org/10.3390/pr11082355

Izadpanah, A. A., & Javidnia, A. (2012). The ability of a nanofiltration membrane to remove hardness and ions from diluted seawater. *Water (Switzerland)*, *4*(2), 283–294. https://doi.org/10.3390/w4020283

Jones, E., Qadir, M., van Vliet, M. T. H., Smakhtin, V., & Kang, S. mu. (2019). The state of desalination and brine production: A global outlook. In *Science of the Total Environment* (Vol. 657, pp. 1343–1356). Elsevier B.V. https://doi.org/10.1016/j.scitotenv.2018.12.076

Labban, O., Liu, C., Chong, T. H., & Lienhard V., J. H. (2017). Fundamentals of low-pressure nanofiltration: Membrane characterization, modeling, and understanding The multi-ionic interactions in water softening. *Journal of Membrane Science*, *521*, 18–32. https://doi.org/10.1016/j.memsci.2016.08.062

Lai, D. Q., Tagashira, N., Hagiwara, S., Nakajima, M., Kimura, T., & Nabetani, H. (2021). Influences of technological parameters on cross-flow nanofiltration of cranberry juice. *Membranes*, *11*(5). https://doi.org/10.3390/membranes11050329

Lu, D., Yao, Z., Jiao, L., Waheed, M., Sun, Z., & Zhang, L. (2022). Separation mechanism, selectivity enhancement strategies and advanced materials for mono-/multivalent ion-selective nanofiltration membrane. In *Advanced Membranes* (Vol. 2). KeAi Communications Co. https://doi.org/10.1016/j.advmem.2022.100032

Ma, Z., Wang, M., Gao, X., & Gao, C. (2014). Charge and separation characteristics of nanofiltration membrane embracing dissociated functional groups. *Frontiers of Environmental Science and Engineering*, *8*(5), 650–658. https://doi.org/10.1007/s11783-013-0605-1

Micari, M., Diamantidou, D., Heijman, B., Moser, M., Haidari, A., Spanjers, H., & Bertsch, V. (2020). *Experimental and Theoretical Characterization of Commercial Nanofiltration Membranes for the Treatment of Ion Exchange Spent Brine*.

Morgante, C., Vassallo, F., Battaglia, G., Cipollina, A., Vicari, F., Tamburini, A., & Micale, G. (2022). Influence of operational strategies for the recovery of magnesium hydroxide from brines at a pilot scale. *Industrial and Engineering Chemistry Research*, *61*(41), 15355–15368. https://doi.org/10.1021/acs.iecr.2c02935

Ojo, O. E., & Oludolapo, O. A. (2025). Innovative recovery methods for metals and salts from rejected brine and advanced extraction processes—A pathway to commercial viability and sustainability in seawater reverse osmosis desalination. In *Water (Switzerland)* (Vol. 17, Issue 21). Multidisciplinary Digital Publishing Institute (MDPI). https://doi.org/10.3390/w17213141

Omerspahic, M., Al-Jabri, H., Siddiqui, S. A., & Saadaoui, I. (2022). Characteristics of desalination brine and its impacts on marine chemistry and health, with emphasis on the persian/arabian gulf: A review. In *Frontiers in Marine Science* (Vol. 9). Frontiers Media S.A. https://doi.org/10.3389/fmars.2022.845113

Popova, A., Rattanakom, R., Yu, Z. Q., Li, Z., Nakagawa, K., & Fujioka, T. (2023). Evaluating the potential of nanofiltration membranes for removing ammonium, nitrate, and nitrite in drinking water sources. *Water Research*, *244*. https://doi.org/10.1016/j.watres.2023.120484

Rismana, E., Arbianto, A. D., & Kusumaningrum, S. (2024). Development of efficient and scalable production process of analytical grade sodium chloride at laboratory scale. *International Journal of Technology*, *15*(3), 743–752. https://doi.org/10.14716/ijtech.v15i3.5606

Roy, Y., Sharqawy, M. H., & Lienhard V., J. H. (2015). Modeling of flat-sheet and spiral-wound nanofiltration configurations and its application in seawater nanofiltration. *Journal of Membrane Science*, *493*, 360–372. https://doi.org/10.1016/j.memsci.2015.06.030

Roy, Y., Warsinger, D. M., & Lienhard, J. H. (2017). Effect of temperature on ion transport in nanofiltration membranes: Diffusion, convection and electromigration. *Desalination*, *420*, 241–257. https://doi.org/10.1016/j.desal.2017.07.020

Saavedra, A., Valdés, H., Velásquez, J., & Hernández, S. (2024). Comparative analysis of donnan steric partitioning pore model and dielectric exclusion applied to The fractionation of aqueous saline solutions through nanofiltration. *ChemEngineering*, *8*(2). https://doi.org/10.3390/chemengineering8020039

Shahgodari, S., Labanda, J., & Llorens, J. (2023). Experimental and modeling study of the nanofiltration of alcohol-based molecules and amino acids by commercial membranes. *Membranes*, *13*(7). https://doi.org/10.3390/membranes13070631

Sri, W., Pratiwi, W., Efendy, M., Nuzula, N. I., Rahem, M., & Afnani, F. (2023). *Production of purified sodium chloride as industrial standart*. https://doi.org/10.21107/juvenil.v4i4.23053

Suhalim, N. S., Kasim, N., Mahmoudi, E., Shamsudin, I. J., Mohammad, A. W., Zuki, F. M., & Jamari, N. L. A. (2022). Rejection mechanism of ionic solute removal by nanofiltration membranes: An overview. In *Nanomaterials* (Vol. 12, Issue 3). MDPI. https://doi.org/10.3390/nano12030437

Szymczyk, A., Lanteri, Y., & Fievet, P. (2009). Modelling the transport of asymmetric electrolytes through nanofiltration membranes. *Desalination*, *245*(1–3), 396–407. https://doi.org/10.1016/j.desal.2009.02.003

Thabo, B., Okoli, B. J., Modise, S. J., & Nelana, S. (2021). Rejection capacity of nanofiltration membranes for nickel, copper, silver and palladium at various oxidation states. *Membranes*, *11*(9). https://doi.org/10.3390/membranes11090653

Tonova, K., Lazarova, M., Dencheva-Zarkova, M., Paniovska, S., Tsibranska, I., Stanoev, V., Dzhonova, D., & Genova, J. (2020). Separation of glucose, other reducing sugars and phenolics from natural extract by nanofiltration: Effect of pressure and cross-flow velocity. *Chemical Engineering Research and Design*, *162*, 107–116. https://doi.org/10.1016/j.cherd.2020.07.030

Yudhi Pamungkas, R., Nurkhamidah, S., Taufany, F., Altway, A., & Rahmawati, Y. (2025). Effect of diethanolamine (DEA) solvent flow rate on the CO_2 absorption-desorption process using a hollow fiber membrane contactor. In *Chemical Engineering Journal e* (Vol. 22, Issue 3).